Materials Advances

ROYAL SOCIETY OF CHEMISTRY

PAPER

View Article Online
View Journal | View Issue

Cite this: *Mater. Adv.*, 2025, 6, 6542

Rare-earth Sm_2O_3-doped SnO_2: tailoring optoelectrical behaviors for a self-driven heterojunction UV-NIR photodetector

Jamal M. Rzaij,[a] Noor F. Khdr Al Attwani,[b] Ethar Yahya Salih *[c] and Mustafa K. A. Mohammed[d]

Received 7th July 2025,
Accepted 5th August 2025

DOI: 10.1039/d5ma00719d

rsc.li/materials-advances

This work elucidates a procedure for the fabrication of novel rare-earth Sm_2O_3-doped SnO_2/Si with tailored optoelectronic characteristics for a self-driven fast-response heterojunction UV-NIR photodetector. The attained optical bandgaps were found to be 3.5 and 3.28 eV with nanoparticle diameters of 54.1 and 52.8 nm, respectively, for undoped SnO_2 and Sm_2O_3-doped SnO_2. The photo-responsive evaluation of the Sm_2O_3-doped geometry revealed strong device functionality in the UV (375 nm) and NIR (808 nm) regions with responsivities of 4.4 and 3.4 mA W^{-1}, respectively, at zero applied bias, indicating the self-biased feature of the proposed geometry; the fabricated photodetector exhibited an I_{SC} value of around 2.5 μA at the mentioned wavelengths. The incident power increment profile indicated a positive correlation with the attained photo-current with an R^2 value of ~0.99. The time-resolved characteristics demonstrated a fast response trend with response/recovery times of 12/50 and 9/18 ms for pristine SnO_2/Si and Sm_2O_3-doped SnO_2/Si, respectively; both devices exhibited stable performance over 10 cycles and 5 days with negligible degradation behavior.

1. Introduction

Silicon (Si)-based optoelectronic technology, photodetection in particular, has gained great interest due to its wide-ranging applications in traditional imaging, biological and environmental research, flame detection, *etc.*[1–5] Additionally, Si-based optoelectronic technology is extensively used because of its cost-effectiveness and exceptional sensitivity within the NIR range.[6–9] However, Si exhibits a relatively narrow optical bandgap (1.1 eV) for which a limited detection ability is attained within the ultraviolet (UV) portion; in UV-based Si detection, short-wavelength's photon is only absorbed *via* relatively shallow surface's depth.[10,11] To overcome this limitation, a hybrid optoelectronic design has emerged, which involves the integration of metal oxides having wide optical bandgaps with a Si wafer in a hetero-/mono-junction framework, where the metal oxide serves the dual functions of a UV absorber and a charge-transport layer.[12] Tin oxide (SnO_2), with an n-type conductivity and a wide bandgap of ~3.7 eV, is widely proven as an excellent transparent conducting oxide in heterojunction frameworks. In heterojunction geometry, SnO_2 is deposited onto a p-type Si wafer forming a p–n junction, where UV light ($\lambda \leq 340$ nm) is absorbed within the SnO_2 layer, which in turn results in electron–hole pair generation; NIR light passes through the Si wafer.[13–15] Doping the metal oxide layer (SnO_2) with rare-earth compounds such as Sm_2O_3 endows tailored optoelectrical characteristics to the p–n heterostructure for higher performance. In detail, the incorporation of Sm^{3+} into the SnO_2 lattice introduces strains and defect states, which could alter the band structure, thereby shifting the absorption cut-off phenomenon of SnO_2 from 340 nm to near-UV region (~400 nm) and probably facilitating a higher charge transfer at the p–n interface.[16,17] Additionally, Sm_2O_3-doped SnO_2 could potentially increase interface passivation and crystalline quality, leading to reduced series resistance and relatively high photocurrent collection efficiency.[18] Furthermore, the introduction of Sm^{3+} into the SnO_2 lattice could result in the reduction of deep trap states that are accountable for persistent photo-conductivity and subsequently a higher rate of carrier concentration.[19] Therefore, Sm_2O_3-doped SnO_2 could allow the tailoring of efficient optoelectronic characteristics with zero applied potential, which in turn enables mobile application. In this study, we report a novel Sm_2O_3-doped SnO_2/Si heterojunction self-driven photodetector for UV-NIR wavelength detection. In detail, the doped heterostructure demonstrated a self-biased feature, especially under UV illumination, with considerable figure-of-merit profiles at zero applied voltage.

[a] *Department of Physics, College of Science, University of Anbar, Anbar, Iraq*
[b] *Laser and optics engineering department, Al-Nahrain University, Baghdad, Iraq*
[c] *College of Energy and Environmental Sciences, Al-Karkh University of Science, Baghdad, 10081, Iraq. E-mail: ethar@kus.edu.iq, ethar988@gmail.com*
[d] *College of Remote Sensing and Geophysics, Al-Karkh University of Science, Baghdad, Iraq*

2. Experimental procedure

In a typical doping procedure, both Sm_2O_3 (Aldrich, 99.99) and SnO_2 (Aldrich, 99.98) were mixed thoroughly with different Sm_2O_3 contents (7% and 9% by weight) using a mortar and pestle using a few drops of ethanol as a binder to support homogeneity and preserve appropriate paste viscosity; this process lasted for about 45 minutes, and the attained mixed powder was then left to dry at 70 °C for 12 hours. The final product was then pressed mechanically into a 2 cm-diameter target pellet under hydraulic press with 5 tones at room temperature. The acquired target was later thermally treated at 500 °C for 1 hour at a heating rate of 5 °C minute^{-1} in an ambient environment. Concurrently, a pre-conditioned p-type Si substrate (Aldrich), diluted with 1% of HF to eliminate native oxide, was positioned within a pulsed laser deposition (PLD) chamber with the prepared target in a vertical alignment and separated by a distance of 5 cm (see Fig. 1); the Si substrate was partially covered to allow later metal electrode deposition on the p-type Si side of the geometry. The placed Sm_2O_3-doped SnO_2 target was subjected to second harmonic 266 nm Nd:YAG pulsed laser with an energy of 700 mJ at an angle of 45°; the laser density, pulse duration, and frequency were set to 55.73 mJ mm^{-2}, 9 nanoseconds, and 6 Hz, respectively. The resulting Sm_2O_3-doped SnO_2 film exhibited a thickness of ~213 nm (Fig. 1); this was primary selected to achieve absorption of light as well as carrier transportation, which, in turn, enables effectual absorption of UV wavelengths. Following the PLD process, a self-powered photodetector geometry was obtained through thermally evaporated Ag metal contact (~10^{-6} mbar).

The morphological and crystal quality analyses of the deposited pristine SnO_2 and Sm_2O_3-doped SnO_2 films were performed using a field emission scanning electron microscope (Hitachi, SU8030, FE-SEM) and an X-ray diffractometer (Bruker, AXS D8, XRD). In conjunction, the optical behavior of the attained films was investigated *via* binary approaches, photoluminescence (PL, Hitachi, SU8030) and ultraviolet visible light (Shimadzu, UV-3600, UV-vis) spectroscopies, while the optical bandgap was estimated using the Tauc relation.[20,21] The optoelectronic properties of the fabricated photodetector were investigated using a source measure unit (SMU, Keithley 2401) incorporating narrow bandpass filters (Thorlabs) to allow monochromatic wavelength transmission. The response/recovery time was estimated from 10% to 90% of the total photocurrent perceived *via* histogram analysis.

3. Results and discussion

Fig. 2(a) displays the XRD patterns of the deposited layers where pristine SnO_2 exhibited a crystalline structure; peaks appearing at $2\theta \approx 26.57°$, 33.87°, 37.85°, 51.65°, 54.62°, and 57.66° are assigned to the planes of (110), (101), (200), (211), (220), and (002), respectively; these corresponded to the tetragonal rutile structure of SnO_2 (JCPDS No. 01-0657). Additionally, the additional peaks appearing around $2\theta \approx 28.45°$ (222) and 47.41° (440) corresponded to the Sm_2O_3 phase, which suggests the efficacious Sm_2O_3 incorporation. Further, a slight peak shift and minor broadening could be due to the size reduction and/or lattice strain, which resulted from Sm^{3+} substitution; this is pre-expected because of ionic radius mismatch ($Sn^{4+} \approx 0.069$ nm; $Sm^{3+} \approx 0.109$ nm) as well as the subsequent defect formation.[22] The optical behavior (Fig. 2b) indicated strong wavelength absorption in the UV region with a slight bathochromic shift towards near visible range for Sm_2O_3-doped SnO_2, indicting tailored optical characteristics of the deposited film. Continuously, the estimated optical bandgap-based Tauc relation for the deposited films exhibited values of 3.5 and 3.28 eV for pristine SnO_2 and Sm_2O_3-doped SnO_2, respectively; this is probably because of the dopant-induced state. The topographies of the deposited films (Fig. 2c and d) revealed a uniform granular structure with compactly packed spherical nanoparticles in the

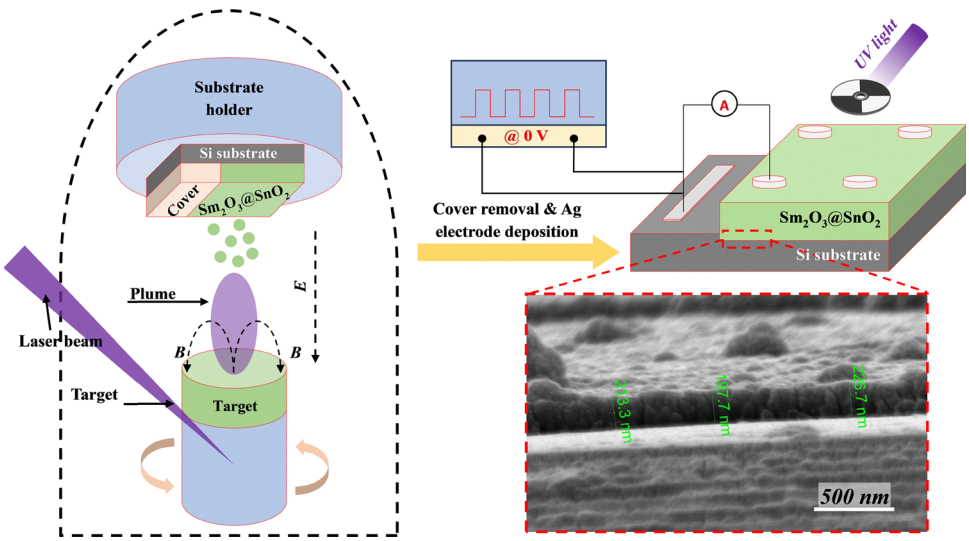

Fig. 1 Graphical representation of the device fabrication procedure.

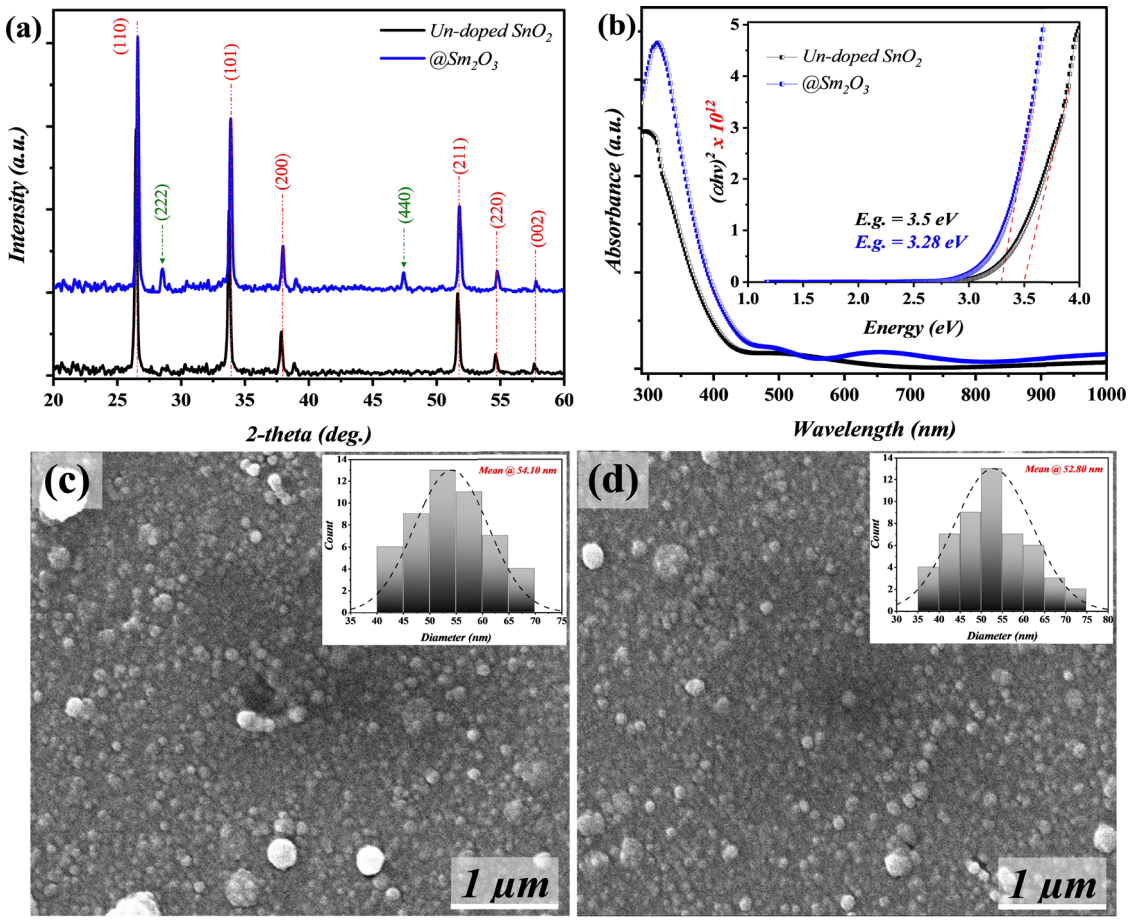

Fig. 2 Characteristics of the deposited films: (a) XRD patterns, (b) UV-vis spectra, and (c) and (d) FE-SEM images of pristine SnO_2 and Sm_2O_3-doped SnO_2, respectively; intsets into (c and d) are nanoparticles' diameter histogram distribution.

range of 1 μm. The average particle diameter (inset of Fig. 2(c and d)) exhibited values of 54.1 and 52.8 nm for the aforementioned films, respectively. The attained slight diameter reduction could result from dopant-induced incorporation during the preparation of grain growth; the reduction in the nanoparticle size upon doping provides potential surface area augmentation, which in turn could be advantageous for sensing application enhancement.

Fig. 3(a and b) present the wavelength-profile *I–V* characteristics of the fabricated heterostructures, where a typical nonlinear rectifying behavior is observed under monochromatic incident light; this confirms the formation of the p–n junction interface with sufficient charge separation derived by a built-in electric field. The attained photocurrent curves mimic wavelength-dependent trends, wherein un-doped SnO_2 and Sm_2O_3-doped SnO_2 devices exhibited the highest *I–V* curve under illumination of 340 and 375 nm corresponding to the absorption cut-off phenomena of the active layer, respectively. This response dependency highlights high UV sensitivity of both devices. The photocurrent curves obtained for the Sm_2O_3-doped SnO_2/Si heterostructure (Fig. 3b) exhibited a relatively high and red-shifted trend as compared to that of the pristine SnO_2 photodetector probably due to the incorporation of Sm^{3+} ions within the SnO_2 lattice. In detail, this incorporation could enable carrier separation *via* the reduction of recombination loss; additionally, Sm_2O_3 introduces a intermediate energy state in the bandgap of SnO_2, which in turn promotes broader spectral response in the near UV region.[23] Further, the *I–V* curve elucidates a noteworthy response under 808 nm illumination, indicating the active role of the used Si wafer in the NIR region; such an observation could be further perceived from the photocurrent profile (Fig. 3c). This designates boosted effectiveness of carrier generation and collection. The self-biased mode of the Sm_2O_3-doped SnO_2/Si heterostructure is attained under two wavelengths (375 and 808 nm; inset of Fig. 3(b)); this confirms the capability of the internal electric field to initiate charge collection at zero external power. Such singularity highlights the effectiveness of Sm_2O_3 doping in improving the photodetection ability of such heterojunction geometry across a broader spectral range. In detail, the self-biased mode attained in the fabricated device is initiated from the built-in potential formed between n-typed oxides and p-type Si wafer. This built-in electric field allows well-organized photo-generated electron–hole pair separation under incident light at zero applied bias voltage. The photo to dark current (I_{ph}/I_D) profile (Fig. 3, d) demonstrated rather superior values for the Sm_2O_3-doped SnO_2/Si photodetector, which also indicates the

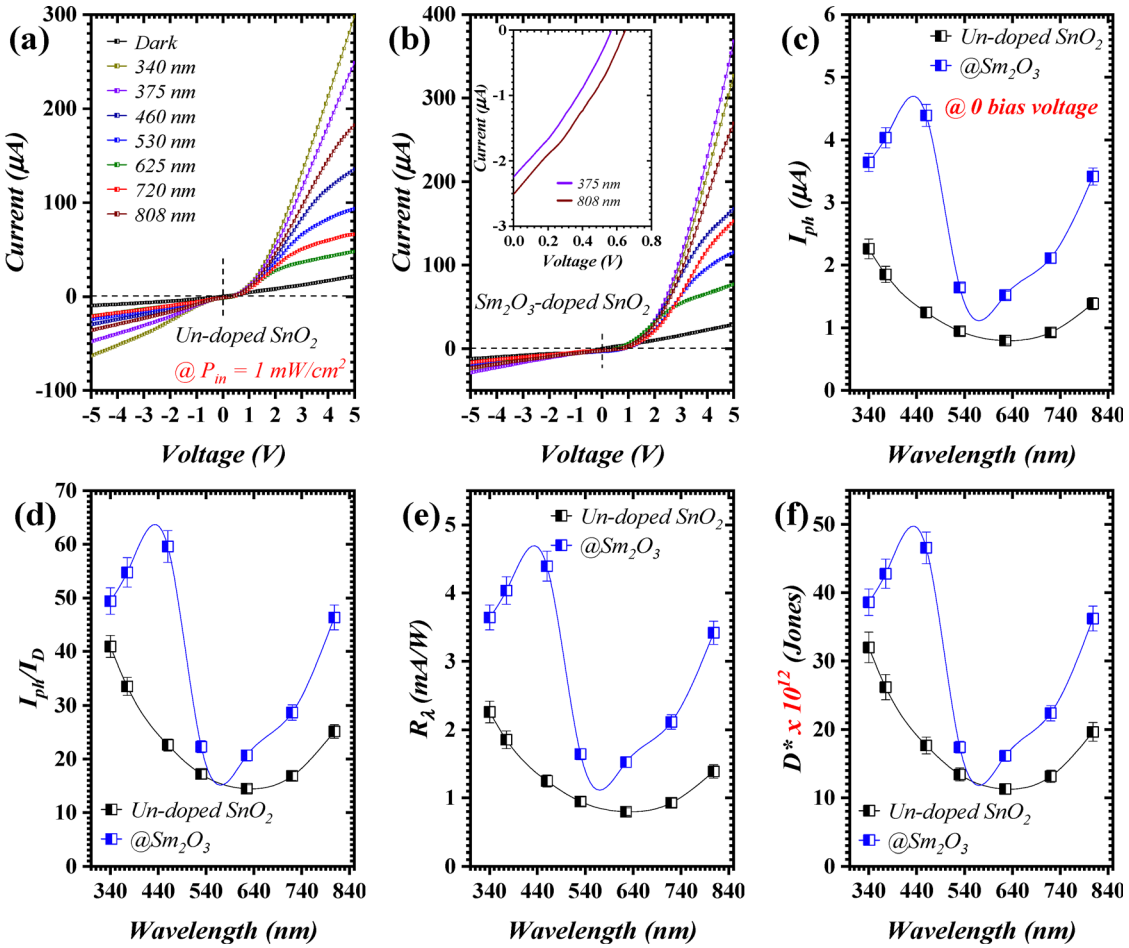

Fig. 3 Wavelength-dependence profile: (a) and (b) *I*–*V* curves, (c) I_{ph}, (d) I_{ph}/I_D, (e) R_λ, and (f) D^* for pristine SnO_2 and Sm_2O_3-doped SnO_2.

active role of Sm_2O_3 doping, reflecting an enhanced signal-to-noise feature (thorough evaluation procedure is demonstrated in Note S1). This improvement proposes highly effective destruction of recombination and condensed leakage under dark conditions by rare-earth doping. The photo-responsivity (R_λ), as a function of wavelength, exhibited a rather high value as well as a spectral coverage range for the Sm_2O_3-doped device, especially under near-UV and NIR illumination with peak values of 4.4 and 3.4 mA W^{-1} at zero bias, which further indicates the self-driven feature of the projected system (Fig. 3 (e)). This further reinforces the assumption that Sm^{3+} positively incorporates the photo-conversion ability. The photo-detectivity (D^*) demonstrated a similar trend to that of R_λ with remarkable noise-limited performance in the UV and NIR regions; the heightened D^* ascends from both lower dark current noise and higher R_λ allowing the proposed Sm_2O_3-doped SnO_2/Si heterostructure for a highly appropriate design for self-biased, low-power, UV-NIR photodetector applications. The presented figure-of-merits were performed at zero bias voltage, which justifies the relatively low figure-of-merit values. However, remarkable performance with considerably higher figure-of-merit values was attained at 5 bias (Fig. S1); R_λ of 0.30 and 0.37 A W^{-1} were attained at 5 V for pristine SnO_2/Si and Sm_2O_3-doped SnO_2/Si heterostructures, respectively.

Fig. 4(a and b) illustrate the *I*–*V* characteristics of the fabricated geometries as a function of incident light intensity; the considered *I*–*V* curves exhibited linear increment as the incident light intensity augmented from 1 to 18 mW cm^{-2}, with respect to the considered photodetector and/or wavelength. This, in turn, confirms the strong photo-conductive behavior of the fabricated geometries. Such linearity could be further observed in the photocurrent profile at zero bias voltage (Fig. 4c), where both devices delivered person correlation values close to unity ($R^2 \approx 1$). This tendency strongly indicates minimal well-organized carrier separation and saturation effects. In term of Sm doping, the Sm_2O_3-doped SnO_2/Si photodetector consistently validates a higher photocurrent profile, which could be due to improved carrier generation enabled through Sm^{3+}-induced trap states.[24] The I_{ph}/I_D ratio (Fig. 4d) demonstrated a similar behavior to that of photocurrent, where the Sm_2O_3-doped SnO_2/Si photodetector outperforms the pristine design, which in turn reflects the condensed dark current as well as higher photo-generated carrier collection productivity. Subsequently, the acquired linearity (R^2 = 0.994) strongly suggests that the fabricated doped device operates in a regime where recombination is insignificant and/or efficiently swept photo-generated carriers by a built-in electric field at zero applied potential. Continuously, the R_λ profile (Fig. 4e)

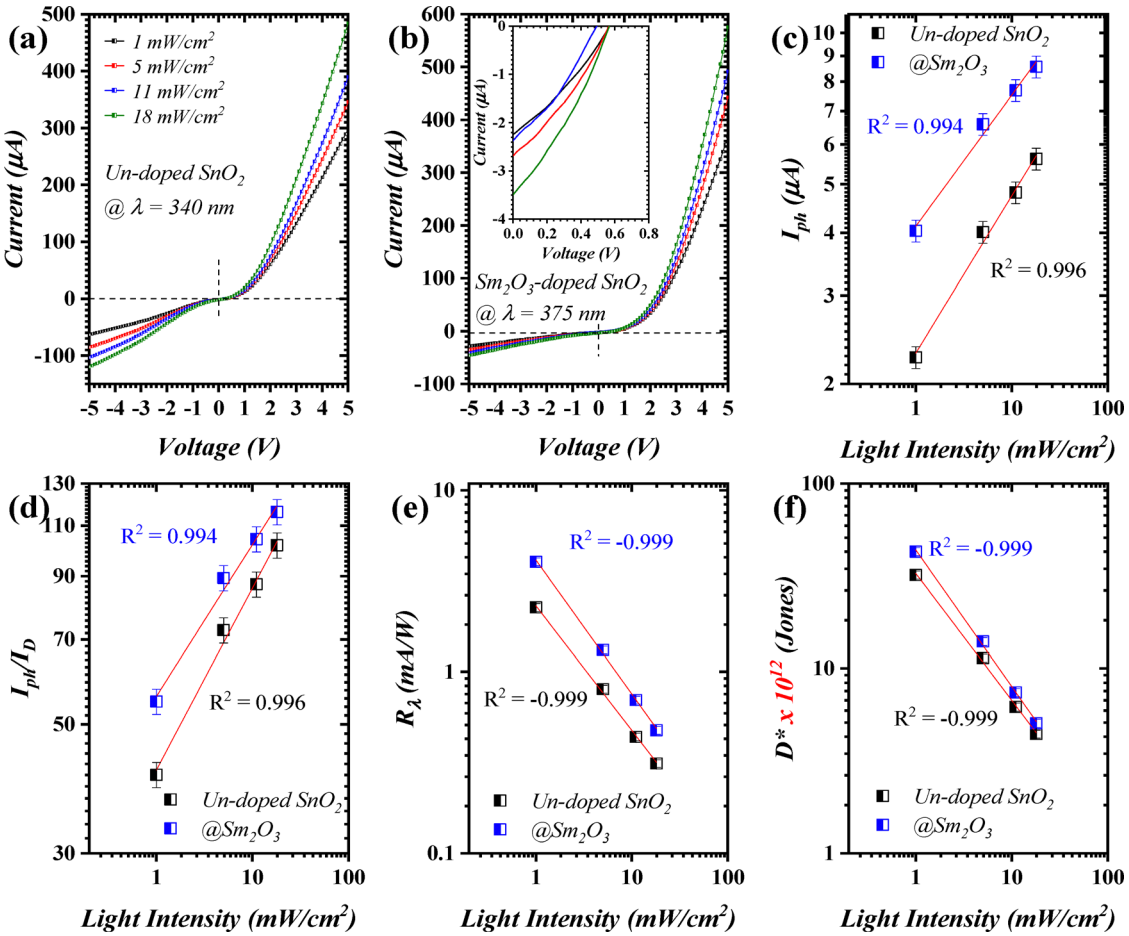

Fig. 4 Illumination intensity-dependence profile: (a) and (b) *I*–*V* curves, (c) I_{ph}, (d) I_{ph}/I_D, (e) R_λ, and (f) *D** for pristine SnO_2 and Sm_2O_3-doped SnO_2.

demonstrated a decreasing trend as a function of incident light intensity, with the value descending from 4.4 to 0.48 mA W^{-1} under illumination of 1 and 18 mW cm^{-2}, respectively, at zero applied bias. The R_λ profile was found to be significantly increased when applied bias introduced; in detail, values of 0.37 and 0.032 A W^{-1} under illumination of 1 and 18 mW cm^{-2}, respectively, see Fig. S2 for further details. This could be justified as the relation between the attained R_λ and incident power density is inversely proportional: $R_\lambda \alpha \frac{1}{P_{in}}$.[25–27] The *D** profile (Fig. 4f) maintained stable and relatively high values across the considered intensities with $R^2 = -0.999$.

Fig. 5(a and b) display the time-resolved feature of both fabricated heterostructures under 10 periodic ON/OFF states with a pulse width of ~5 s under zero bias conditions. Both pristine SnO_2/Si and Sm_2O_3-doped SnO_2/Si photodetectors exhibited stable switching behaviors over multiple cycles with insignificant baseline shift or degradation. However, the undoped photodetector (Fig. 5a) delivered low photo-current as compared to that doped with Sm_2O_3, indicating ineffective photo–carrier separation and transport. The enhanced photo-current in the doped device (Fig. 5b) indicates the active role of Sm doping, which directly improves the charge extraction efficiency allowing greater self-powered action. Additionally, the Sm_2O_3-doped SnO_2/Si photodetector exhibited faster switching characteristics with a response/recovery time of 9/18 ms, while the pristine SnO_2/Si photodetector demonstrated values of 12/50 ms, which could be attributed to enhanced carrier mobility and reduced trap density, indicating tailored optoelectronic characteristics. Further, both devices revealed a faster rise time as compared to that of fall, which in turn indicates faster carrier generation than recombination. The fabricated photodetectors showed stable switching cycles over 5 days (Fig. S3b and S4b). The time-resolved characteristics were also investigated in terms of incident light intensity (Fig. S3c and S4c); the related outcomes indicate a positive linear correlation with the applied light intensity with an R^2 value close to unity.

Fig. 6 depicts the energy band alignment between p-type Si and n-type SnO_2 with a type-II staggered heterojunction with CB and VB offsets of ≈0.35 and 2.86 eV, respectively. An extra defect-induced donor state is formed near the edge of CB upon Sm_2O_3 doping, which resulted in enhanced carrier generation. As a result, the built-in band bending across the depletion region allows electron–hole pair separation at zero applied bias. In detail, Sm^{3+} incorporation into the SnO_2 lattice delivers lattice strain and oxygen vacancy because of the mismatch of ionic radius between rare-earth dopant (Sm^{3+}) and Sn^{4+}. This rare-earth-induced defect could create intermediate energy level/s, which in turn promotes sub-bandgap and then a higher ratio of

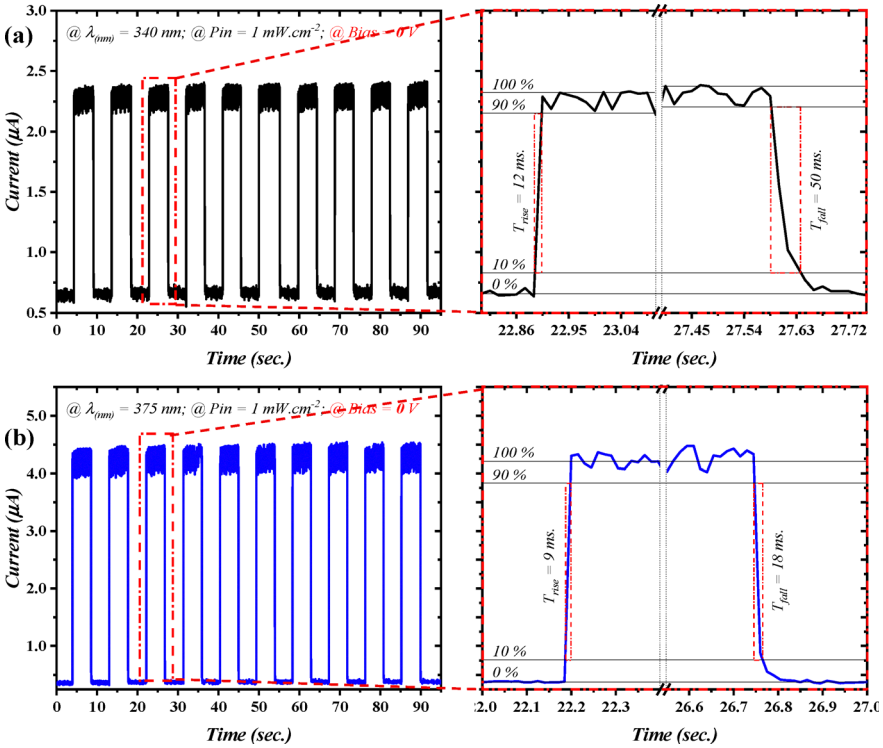

Fig. 5 Time-resolved characteristics: (a) pristine SnO_2 and (b) Sm_2O_3-doped SnO_2.

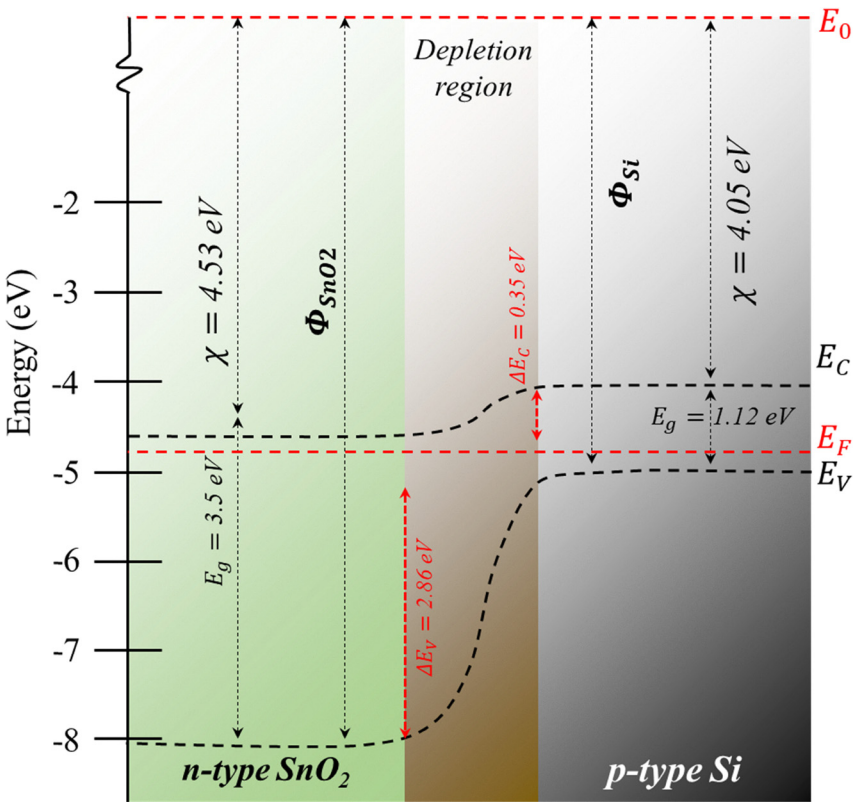

Fig. 6 Energy band diagram of the SnO_2/Si heterostructure.

Table 1 Comparison of the projected design with similar geometries reported

Design	Potential (V)	λ_{nm}	R_λ (mA W^{-1})	D^* (Jones)	T_{rise}/T_{fall} (ms)	Ref.
SnO_2/Si	3	340	33	1×10^{15}	290/310	28
CdS-SnO_2/Si	—	635	3.7	2.13×10^{7}	—	29
MoS_2-SnO_2/Si	—	635	3.0	1.16×10^{7}	—	29
Nd-SnO_2	15	275	129	5.84×10^{9}	5.33/5.63	30
Zn-SnO_2	—	—	3.6	9.04×10^{7}	—	31
GeO_2-SnO_2/Si	3	365	0.36	—	400/650	32
SnO_2/Si	0	340	3.4	3.2×10^{13}	12/50	This work
Sm_2O_3-SnO_2/Si	0	375	4.4	4.3×10^{13}	8/18	This work

free carrier density. Moreover, such defect state assists in enabling a higher number of photogenerated carriers at the junction interference as well as a possible recombination rate reduction, which leads to improved time-resolved characteristics.[16,17]

The proposed geometry, using rare-earth doping, demonstrated rather considerable outcomes as compared to other reported devices; the related comparison is demonstrated in Table 1.

4. Conclusion

The integration of rare earth Sm_2O_3 into a SnO_2 matrix as a self-biased heterojunction for a UV-NIR photodetector was successfully demonstrated by PLD technique. The microstructural and optical analysis indicated reduction of 2.3 nm and 0.22 eV, respectively. The fabricated device (Sm_2O_3-doped SnO_2/Si) demonstrated a dual functionality in near-UV (375 nm) and NIR (808) regions. In particular, at zero bias voltage, the proposed geometry exhibited R_λ of 4.4 and 3.4 mA W^{-1}, respectively. Meanwhile, perceived R_λ delivered remarkably higher values under 5 V applied bias (0.37 and 0.27 A W^{-1}). The fabricated photodetectors demonstrated linear I_{ph} increment as a function of the incident light intensity with an R^2 value close to unity ($R^2 \approx 1$). Despite the long-term stability-based time-resolved feature, the response/recovery time was found to be 12/50 and 9/18 ms for pristine SnO_2/Si and Sm_2O_3-doped SnO_2/Si, respectively.

Author contributions

E. Y. S. comprehended the geometry of the heterostructure along with its fabrication procedure. M. K. A. M. and E. Y. S. performed the heterostructure optoelectronic capacity and associated performance investigations. J. M. R. and N. F. K. A. executed the structural, morphological, and optical examination and their analysis. All named authors contributed correspondingly to the preparation and discussion of the article.

Conflicts of interest

There are no conflicts to declare.

Data availability

All the data used are presented in the manuscript.

Supplementary information available: Figures-of-merit evaluation (Note S1) wavelength dependent figures-of-merit at 5 V (Fig. S1), incident light intensity dependent at 5 V (Fig. S2), time-resolved characteristics of pristine SnO_2/Si and Sm_2O_3-doped SnO_2/Si (Fig. S3 and S4), respectively. See DOI: https://doi.org/10.1039/d5ma00719d

References

1 L. Shi and S. Nihtianov, Comparative study of silicon-based ultraviolet photodetectors, *IEEE Sens. J.*, 2012, **12**(7), 2453–2459.
2 H. A. Radwan, *et al.*, ZnO/PSi nanoparticles thin film for NO2 sensing application prepared by pulsed laser deposition, *Indian J. Phys.*, 2024, **98**(2), 455–467.
3 Y.-C. Huang, *et al.*, Silicon-based photodetector for infrared telecommunication applications, *IEEE Photonics J.*, 2021, **13**(2), 1–7.
4 A. Mohammed Enad and J. M. Rzaij, Synthesis of CuO Thin Film Incorporated with Nanostructured Nd_2O_3 Deposited by Pulsed Laser Deposition for Ammonia Sensing Applications, *Nano*, 2025, **20**(03), 2450113.
5 M. K. Mohammed, *et al.*, Facile synthesis of chitosan-MoS2 over reduced graphene oxide to improve photocatalytic degradation of methylene blue, *J. Sol-Gel Sci. Technol.*, 2024, 1–11.
6 R. W. Keyes, Fundamental limits of silicon technology, *Proc. IEEE*, 2002, **89**(3), 227–239.
7 C. Liu, *et al.*, Silicon/2D-material photodetectors: from near-infrared to mid-infrared, *Light: Sci. Appl.*, 2021, **10**(1), 123.
8 T. Yu, *et al.*, Highly polarization-sensitive narrowband near-infrared photodetection by all-silicon embedded plasmonic hot electron devices, *ACS Photonics*, 2025, DOI: 10.1021/acsphotonics.5c00379.
9 M. K. Modhi and J. M. Rzaij, Synthesis and characterization study of CuO thin film and CuO-CeO_2 nanostructured composite using chemical spray pyrolysis, *AIP Conf. Proc.*, 2023, **2591**, 030066.
10 X. Wan, *et al.*, A self-powered high-performance graphene/silicon ultraviolet photodetector with ultra-shallow junction: breaking the limit of silicon?, *npj 2D Mater. Appl.*, 2017, **1**(1), 4.
11 J. Yin, *et al.*, Engineered tunneling layer with enhanced impact ionization for detection improvement in graphene/silicon heterojunction photodetectors, *Light: Sci. Appl.*, 2021, **10**(1), 113.
12 L. Sang, M. Liao and M. Sumiya, A comprehensive review of semiconductor ultraviolet photodetectors: from thin film to one-dimensional nanostructures, *Sensors*, 2013, **13**(8), 10482–10518.

13 E. P. de Araújo, *et al.*, A study of visible-blind properties of a SnO_2's nanowires network photodetector, *Eng. Proc.*, 2021, **6**(1), 40.
14 X. Li, *et al.*, Facile construction of p-Si/n-SnO_2 junction towards high performance self-powered UV photodetector, *J. Semicond.*, 2025, **46**(7), 072701-1.
15 E. T. Salim, *et al.*, The unclad single-mode fiber-optic sensor simulation for localized surface plasmon resonance sensing based on silver nanoparticles embedded coating, *Plasmonics*, 2024, **19**(1), 131–143.
16 I. Apostolova, A. Apostolov and J. Wesselinowa, Band gap tuning in transition metal and rare-earth-ion-doped TiO_2, CeO_2, and SnO_2 nanoparticles, *Nanomaterials*, 2022, **13**(1), 145.
17 H. Xu, *et al.*, Effect of rare earth doping on electronic and gas-sensing properties of SnO_2 nanostructures, *J. Alloys Compd.*, 2022, **909**, 164687.
18 P. Senthilkumar, *et al.*, Enhanced optoelectronic and catalytic properties of Sm doped SnO_2 thin films, *Phys. B*, 2024, **690**, 416208.
19 G. Charrada, *et al.*, Synthesis of Sm-Doped CuO–SnO_2: FSprayed Thin Film: An Eco-Friendly Dual-Function Solution for the Buffer Layer and an Effective Photocatalyst for Ampicillin Degradation, *Technologies*, 2025, **13**(5), 197.
20 A. Ibraheam, J. M. Rzaij and M. M. Arshad, Influence of Magnesium Content on the Structural, Optical, and Electrical Properties of $Cu_2(Zn_{1-x}Mg_x)$ SnS_4 Nanostructured Quaternary Thin Film Synthesized Using the Sol–Gel Method, *J. Electron. Mater.*, 2023, **52**(1), 414–421.
21 J. M. Rzaij, Q. A. Abbas and A. M. Khalaf, Investigating the structural, topographical, morphological and optical effects of AgO on sprayed SnO_2 thin films, *Bull. Mater. Sci.*, 2023, **46**(4), 200.
22 V. Agrahari, *et al.*, Low field room temperature magnetism and band gap modifications in Sm doped SnO_2, *J. Mater. Sci.: Mater. Electron.*, 2016, **27**, 3053–3064.
23 H. M. Aliha, A. A. Khodadadi and Y. Mortazavi, The sensing behaviour of metal oxides (ZnO, CuO and Sm_2O_3) doped-SnO_2 for detection of low concentrations of chlorinated volatile organic compounds, *Sens. Actuators, B*, 2013, **181**, 637–643.
24 L. Singh, M. N. Luwang and S. Srivastava, Luminescence and photocatalytic studies of Sm^{3+} ion doped SnO_2 nanoparticles, *New J. Chem.*, 2014, **38**(1), 115–121.
25 S. A. Khalaf, *et al.*, Photoresponse Evaluation of a Multiband Self-Driven SnO_2/CuO/Si Heterojunction Photodetector Fabricated by Pulsed Laser Deposition, *ACS Appl. Electron. Mater.*, 2025, **7**(8), 3409–3415.
26 E. Y. Salih, *et al.*, Fast-response self-powered double-heterojunction n-ZnO/p-ZnTe/n-Si photodetector, *Nanoscale Adv.*, 2025, DOI: **10.1039/D5NA00331H**.
27 E. A. Abed, *et al.*, Fabrication and dual-band detection evaluation of dye-sensitized ZnO photodetector, *Mater. Lett.*, 2025, **391**, 138513.
28 E. Y. Salih, Opto-electrical evaluation of visible blind fast-response nanostructured SnO_2/Si photodetector, *RSC Adv.*, 2024, **14**(38), 27733–27740.
29 S. Rahman, *et al.*, Role of temperature on CdS and MoS_2 doped SnO_2 nanostructures: Potential applications in photodetection and temperature dependent current-voltage characteristics, *J. Alloys Compd.*, 2023, **941**, 168901.
30 C. Han, *et al.*, The role of Nd doping in defect compensation and performance enhancement of SnO_2 ultraviolet photodetectors, *J. Alloys Compd.*, 2025, **1016**, 178910.
31 W.-J. Lee, *et al.*, Persistent photoconductivity control in Zn-doped SnO_2 thin films for the performance enhancement of solar-blind ultraviolet photodetectors, *ACS Photonics*, 2023, **10**(11), 3901–3914.
32 S. O. Abdulghani, E. Y. Salih and A. S. Mohammed, Fabrication and photo-responsive characteristics of GeO_2 doped SnO_2/porous Si film for ultraviolet photodetector application, *Mater. Chem. Phys.*, 2023, **303**, 127859.